Audio Engineering Society

Convention Paper

Presented at the 119th Convention
2005 October 7–10 New York, NY, USA

Radiated sound field analysis of loudspeaker systems: discrete geometrical distribution of circular membranes versus co-incident annular rings

Bernard G.A. DEBAIL[1], and Hmaied SHAIEK[2]

[1] *Cabasse Acoustic Center, Plouzané, 29280, France*

[2] *GET, ENST Bretagne Département SC, CNRS TAMCIC, Technopôle Brest-Iroise - CS 83818 29238 Brest Cedex 3, France*

Correspondence should be addressed to Bernard, Hmaied (`bernard.debail@cabasse.com`, `hmaied.shaiek@enst-bretagne.fr`)

ABSTRACT

This paper addresses the problem of the spatial distribution of sound pressure generated by an annular membrane. A generalized theoretical approach will be developed in order to predetermine the sound field radiation of a disc or ring shaped diaphragm, placed on a rigid infinite baffle. Because no assumption is made regarding the observing point, this generalized method is able to predict the acoustic pressure not only in the far field region but also in near field. Results demonstrate the superiority of the co-incident ring distribution compared to the traditional discrete distribution of discs. A new transducer based on concentric rings and disc especially designed to respect this coincident criterion will be introduced.

1. INTRODUCTION

Several examples of co-axial and co-incident sources [1], [2], [3], have demonstrated the advantage of this configuration in terms of time alignment, phase shift deviation and lobbing compared to the traditional discrete geometrical distribution of transducers. A common way to deal with this topic in the literature consists in determining the frequency response off-axis and/or the directivity pattern of the drivers in the far field region.

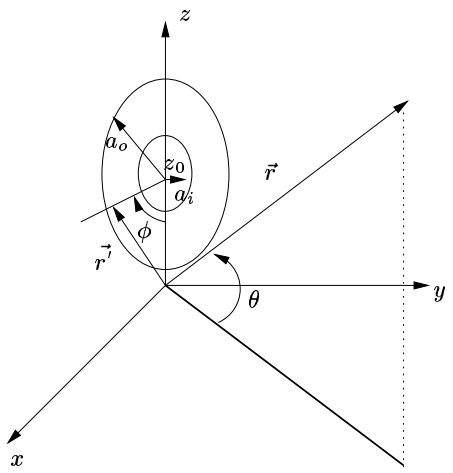

Fig. 1: Position of the ring in a cartesian coordinate

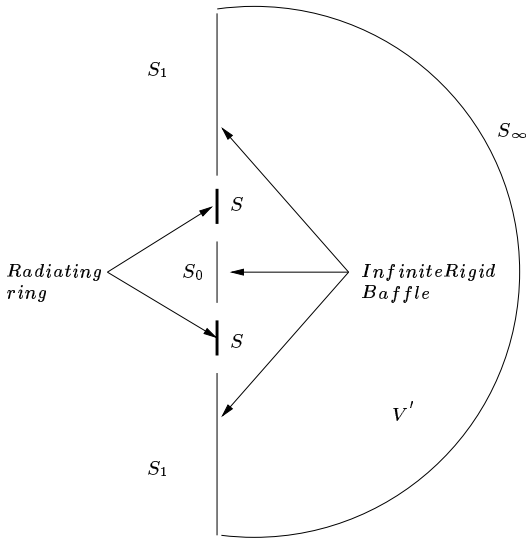

Fig. 2: Domain of integration

However, these data do not provide enough description of the radiated field especially when the near field is concerned and when multiples drivers are involved.

We propose in this paper a theoretical survey based on the interaction of the fields radiated by driver systems, comparing a discrete source distribution with a co-incident one. For this purpose and in order to get a better insight into the radiated field, a $2D$ map description of the pressure field will be presented.

2. THEORETICAL APPROACH

2.1. Sound radiation model

Let consider that the disc or ring will be referenced into space in a cartesian coordinate with the symbols depicted in figure 1.

The ring of internal diameter $2a_i$ and outside diameter $2a_o$ is actuated by a sinusoidal driving force and located on an infinite baffle. Our target is to determine the sound pressure level induced by the sources at a given location. The ring is located on the (Ox, Oz) plane and its center cross the z axis at an altitude z_0. The sound wave propagation is submitted to physical laws which are described by the state equation, Euler equation and the mass preservation equation. The combination of these different equations leads to the sound wave equation. In the case of a sine wave, this equation becomes [4]:

$$\Delta p(\vec{r}) + k^2 p(\vec{r}) = div\vec{f}(\vec{r}) \quad (1)$$

with $k = \frac{\omega}{c}$, the wave number, $\omega = 2\pi f$, the pulsation, f , the frequency and c the speed of sound in the air. $\vec{f}$ is the force vector per unit volume. The solution of equation (1) is given by the Helmholtz-Huygens equation [4]:

$$p(\vec{r}) = -\int\int\int_{V'} G(\vec{r},\vec{r'}) div\vec{f}(\vec{r'}) dV' + \int\int_{S'} [G(\vec{r},\vec{r'})\frac{d}{dn}p(\vec{r'}) - p(\vec{r'})\frac{d}{dn}G(\vec{r},\vec{r'})]dS' \quad (2)$$

where V' , S' and G are respectively the volume area, surface area and Green function which need to be defined. The vector $\vec{n}$ is a vector normal to the surface concerned and the Green function should satisfy the following inhomogeneous Helmholtz equation :

$$\Delta G(\vec{r},\vec{r'}) + k^2 G(\vec{r},\vec{r'}) = -\delta(\vec{r} - \vec{r'}) \quad (3)$$

where δ is the Dirac function. $\vec{r'}$ refers to the location of point on the pertaining surface of volume area. In the case of our survey, the integration domain will be chosen as depicted in figure 2.

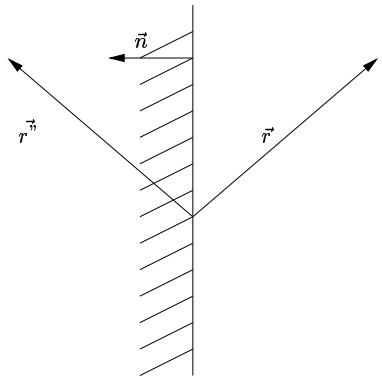

Fig. 3: Image method

S_0 corresponds to the surface of a rigid circular baffle inside the radiating ring of surface S, while S_1 is the surface area of the infinite baffle and S_∞ is the surface area of the half-sphere of infinite radius. The infinite volume limited by the surface $S^{'} = S_0 + S + S_1 + S_\infty$ is named $V^{'}$. The action of the radiating ring is introduced as a limit condition, the sound propagation can be considered as homogeneous and the volume integral consequently disappears as no sources is located inside the volume $V^{'}$.

To solve the problem, we will choose a Green function which its derivative normal to the surface equals zero on the (Ox, Oz) plane as shown in figure 3.

Using the preceding formulation, the Green function chosen can be expressed as follow [6]:

$$G(\vec{r},\vec{r'}) = \frac{1}{4\pi}\frac{e^{-jk|\vec{r}-\vec{r'}|}}{|\vec{r}-\vec{r'}|} + \frac{1}{4\pi}\frac{e^{-jk|\vec{r}-\vec{r''}|}}{|\vec{r}-\vec{r''}|} \quad (4)$$

Equation (2) becomes:

$$p(\vec{r}) = -\int\int_{S'} G(\vec{r},\vec{r'})\frac{d}{dy}p(\vec{r'})dS' \quad (5)$$

The surface integral over S_∞ is null because of the Sommerfeld condition [6]. Additionally, the baffle being infinitely rigid, the normal velocity $v_b \propto \frac{dp}{dy}(\vec{r'})$ is null all along the baffle surface. Equation (5) leads therefore to:

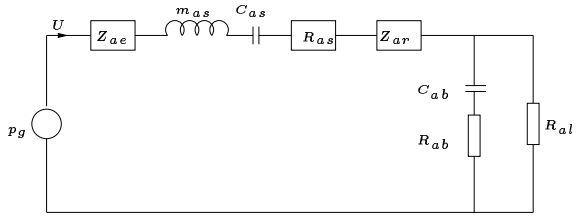

Fig. 4: Lumped papramter acoustical analogy

$$p(\vec{r},a_o,a_i) = \int\int_{S'} \frac{e^{-jk|\vec{r}-\vec{r'}|}}{2\pi|\vec{r}-\vec{r'}|}jk\rho c v(\vec{r'})dS = \frac{jk\rho c}{2\pi}\int_0^{2\pi} d\phi \int_{a_i}^{a_o} \frac{e^{-jk|\vec{r}-\vec{r'}|}}{|\vec{r}-\vec{r'}|}v(\vec{r'})ada \quad (6)$$

In the case of a disc, $a_i = 0$ and the integral becomes the already known Huygens-Rayleigh integral $p(\vec{r},a_0,0)$ of a disc of diameter $2a_o$ located on a infinite baffle. Note that $p(\vec{r},a_o,a_i) = p_(\vec{r},a_o,0) - p_(\vec{r},0,a_i)$. The physical interpretation is trivial.

For our survey, even if the assumption is strong, we will consider that the ring vibrates in a piston-like motion meaning that the velocity will be uniform all along its surface area. In practice, this assumption is reasonable as long as the dimensions of the disc are negligible in regards to the wavelength of the bandwidth concerned. As a result, lumped parameter equivalent circuit [7] will be used to evaluate the velocity frequency response of the ring.

2.2. Equivalent lumped parameter circuit

In the domain concerned $V^{'}$, the ring will radiate on a single face due to the infinite baffle. In order to confront the theoretical simulations with experimental results, closed box sources without port tube will be considered. Figure 4 shows the lumped parameter circuit in the acoustic analogy with the following glossary:

p_g: equivalent pressure source of the generator (amplifier)

U: volume velocity of the ring diaphragm

Z_{ae}: equivalent acoustic impedance of the voice coil and generator electric impedance

m_{as}: acoustic mass of the ring diaphragm

C_{as}: acoustic compliance of the ring diaphragm

R_{as}: acoustic resistance of the ring diaphragm

Z_{ar}: acoustic radiation impedance of the ring diaphragm in an infinite baffle (see appendix)

C_{ab}: acoustic compliance of the enclosed volume V_b of the enclosure

R_{ab}: acoustic resistance of the enclosure losses due to internal energy absorption

R_{al}: acoustic resistance of the enclosure losses due to leakage losses.

with

$$p_g = \frac{e_g Bl}{S(R_g + Z_e)} \tag{7}$$

and

$$Z_{ac} = (\frac{Bl}{S})^2 \frac{1}{R_g + Z_e} \tag{8}$$

where

e_g: output open voltage of the generator (amplifier)

Bl: force factor of the drive unit

R_g: electrical resistance of the generator (amplifier)

Z_e: electrical impedance of the voice coil with $Z_e = R_{cc} + j\omega L_e$

R_{cc}: electrical resistance of the voice coil

L_e: electrical inductance of the voice coil

The velocity of the diaphragm can be extracted from the expression of the volume velocity U going through the circuit:

$$v = \frac{U}{S} = \frac{\frac{p_g}{S}}{Z_{ac} + R_{as} + j\omega m_{as} + Z_{ar} + \frac{1}{\frac{1}{R_{al}} + \frac{1}{R_{ab} + \frac{1}{j\omega C_{ab}}}}} \tag{9}$$

After development, we obtain:

$$v = \frac{1}{S} \frac{j\omega C_{as}[1 + j\omega(R_{ab} + R_{al})C_{ab}]p_g}{1 + j\omega b_1 + j(\omega)^2 b_2 + j(\omega)^3 b_3} \tag{10}$$

with :

$b_1 = C_{as}(Z_{ae} + R_{as}) + C_{as}R_{al}$
$b_2 = C_{as}m_{as} + C_{as}C_{ab}(R_{al}R_{ab} + (R_{al} + R_{ab})(Z_{ae} + R_{as}))$
$b_3 = (R_{al} + R_{ab})C_{ab}C_{as}m_{as}$

In the case of this survey, we will consider $R_{al} = Q_b\sqrt{m_{as}/C_{ab}}$ with $Q_b = 7$ (quality factor of the enclosure), $m'_{as} = m_{as} + \Re(Z_{ar})$ where $\Re(Z_{ar})$ is the real part of Z_{ar} and $R_{ab} = 0$.

3. SIMULATIONS AND EXPERIMENTAL RESULTS

3.1. Position of the problem

As a full range driver with a good overall performance is hard to achieve, most High-Fidelity loudspeaker systems are of the multi-way type. Therefore, two or more drive units must be used, each designed for optimum performance over a limited frequency range.

In most conventional loudspeaker systems, transducers have discrete distribution and are physically separated. Alternatively they are co-axially mounted.

The first co-axial loudspeaker system was developed by Altec-Lansing and Tannoy in 1940 and has not changed much since then with Olson and May models [1], [2], [3] and [5]. It was a two way loudspeaker with a low frequency drive-unit mounted behind a high frequency one. These solutions still show diffractions problem and axial delays due to front back drivers separation.

3.2. Co-axially versus discreetly distributed transducers: description of theoretical models

In this paragraph, the problem of drivers physical distribution in multi-way loudspeaker systems will be addressed. The loudspeaker is made up with three drivers, each designed for optimum performance over its specific frequency band. For clarity reasons, the following terminology will be used :

- $Low - mid$: transducer dedicated to low medium frequencies reproduction $f \leq 820Hz$.
- $Upper - mid$: transducer dedicated to high medium frequencies reproduction $820Hz \leq f \leq 4100Hz$.

- *Tweeter* : transducer dedicated to high frequencies reproduction $f \geq 4100Hz$.

$f_1 = 820Hz$ and $f_2 = 4100Hz$ are commonly called crossover frequencies.

We will consider here two three-way loudspeaker systems : system 1 and system 2, placed on an infinite rigid baffle.

3.2.1. System 1 : Loudspeaker system with coaxially distributed transducers

System 1 consists in a 3 way system with driver co-axially mounted. The Tweeter is a disc of diameter $d_{tw} = 28mm$ surrounded by the Upper-mid concentric radiating ring with an outside diameter of $d^o_{um} = 106mm$ and inside diameter of $d^i_{um} = 43mm$. The previous drivers constitute the $BC13$ unit mounted inside the Low-mid ring with an outside diameter of $d^o_{lm} = 204mm$ and an inside diameter of $d^i_{lm} = 124mm$.

For this model, we suppose flat and co-planar membranes. Also, the space between the inter-drivers spacing is due to practical constraints in the design of this loudspeaker system and is part of the infinite baffle.

3.2.2. System 2 : Loudspeaker system with discreetly distributed transducers

It is an acoustically equivalent loudspeaker to system 1 with three flat and co-planar radiating discs discreetly distributed. The Tweeter unit is the same as the one used for system 1. The Upper-mid driver is here a disc of equivalent diameter d^{eq}_{um} calculated to give the same radiating surface of the Upper-mid used in system 1. d^{eq}_{um} is given by equation (11):

$$d^{eq}_{um} = \sqrt{(d^o_{um})^2 - (d^i_{um})^2} = 96mm \qquad (11)$$

The same approach is used to obtain the equivalent Low-mid diameter d^{eq}_{lm} given by equation (12):

$$d^{eq}_{lm} = \sqrt{(d^o_{lm})^2 - (d^i_{lm})^2} = 162mm \qquad (12)$$

In order to reduce interference problems between transducers, the inter-drivers spacing has been minimized considering the practical dimensions of the frames of the drive units. This constraint lead to a

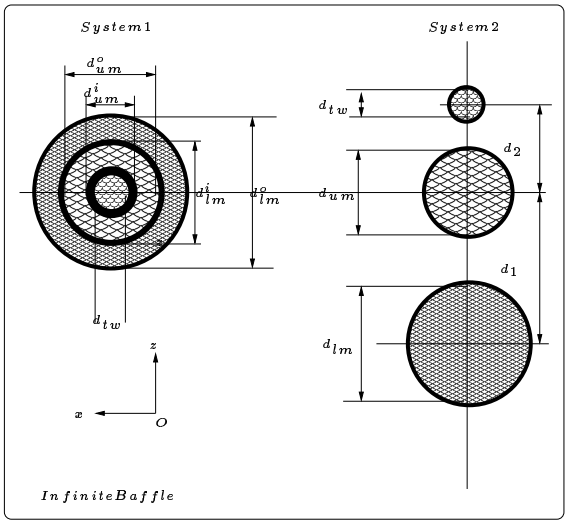

Fig. 5: Co-incident and discrete geometrical distribution description

spacing $d_1 = 212mm = \lambda_1/2$ between the Low-mid and the Upper-mid units. However the Upper-mid-Tweeter spacing is $d_2 = 125mm = 3\lambda_2/2$. λ_1 and λ_2 are the wave length relative to f_1 and f_2.

The above description can now be summarized in figure 5 where the two loudspeakers are placed in the (Ox, Oz) infinite rigid baffle and radiated in 2π steradian solid angle.

In practice, the baffle can not be infinite. Our measurements were made using a finite rectangular baffle given in figure 6. The measurements have been proceeded in free field conditions with the microphone placed at a distance of $1.5m$ from the source.

3.3. Crossover network

In multi-way loudspeaker systems, we must avoid band overlap and prevent each driver from being fed frequencies outside its calibrated operating region. Thus, a suitable filter bank is employed to divide the input signal into several bands. This network is known as loudspeaker crossover.

Crossover filters are traditionally implemented with analog electronics. They may take the form of a passive network interposed between the power amplifier and the drivers. Alternatively, they can be placed before the power amplifier in an active approach. Ideally crossover filters should have band

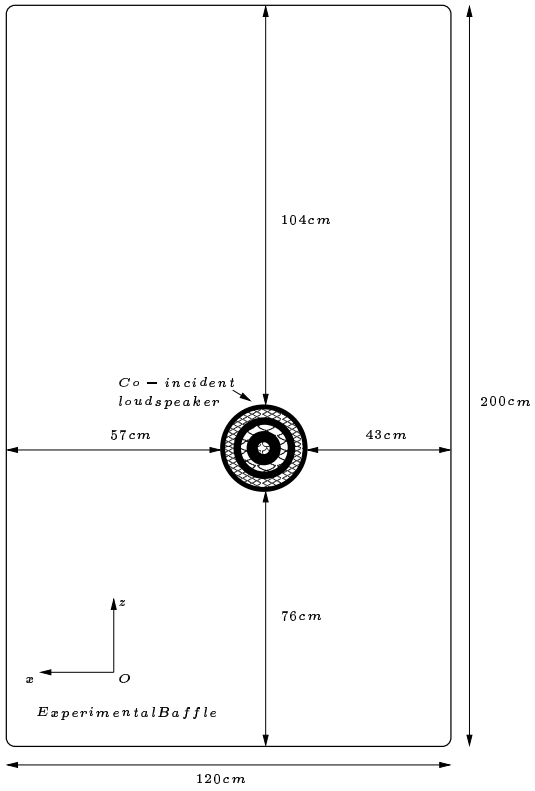

Fig. 6: Size of the baffle used in the experimental set-up

pass frequency domain characteristics, high cut-off rates and an overall response with flat amplitude and linear phase. Using digital filters, we can satisfy all the above properties in one filter bank structure [8], [9].

Digital crossover is a new approach that has emerged within the last few years [8], [10], [11], [12], [13]. This is in fact an active crossover, but with the filter segments implemented digitally using generally FIR linear phase filters. This filter structure is always stable, which is a suitable criterion for real time implementation. We have decided to use this crossover type in our experiment in order to both limit the interference issue to minimal (thanks to the high cut-off rate) and guarantee that the crossover will not add any phase shift around the cut-off frequency f_1 and f_2 other than a pure time delay.

Around each crossover frequencies f_1 and f_2, a pair of low pass/high pass linear phase filters sends to each drive unit a portion of the input signal that can be reproduced with the least distortion. The low-pass crossover filter can be obtained by using one of the established digital filter design techniques (windowing, frequency sampling or optimal design algorithms). After a comparative study of different techniques [8], we decided to use the Kaiser Window method since it allows a trade off between the width of the transition region and the peak ripple amplitude to be achieved. The filter order was adjusted to achieve cut-off rates of $24dB$ per octave around these frequencies. Additional high-pass respectively low-pass filters at $100Hz$ respectively $20kHz$ was included to cut-off extremely low and high frequencies at $12dB$ per octave. The resulting crossover filters have different lengths and the overall filter bank response shows amplitude anomalies around crossover frequencies. We can easily overcome this problem by introducing extra delays through the path of the filters in advance.

The phase delay between two linear phase filters of N_1 and N_2 taps (with $N_1 > N_2$) is given by :

$$\tau = \frac{N_1 - N_2}{2f_s} \tag{13}$$

where f_s is the sampling frequency.

This procedure garentees equal group delays over the three frequency band of interest. As we can see from

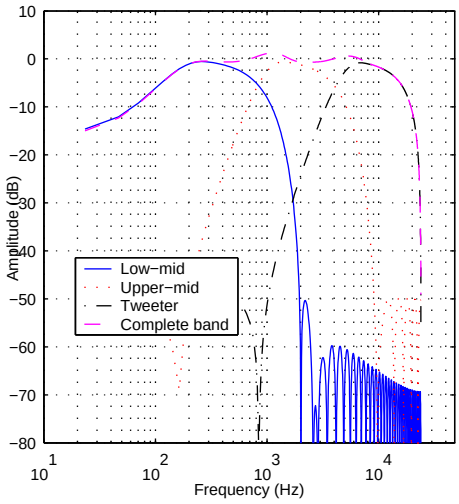

Fig. 7: Crossover filter bank

figure 7, the crossover filter bank provides nearly flat amplitude responses.

The crossover filter bank will now be applied to the on-axis responses of system 1 and 2. Figure 8 shows the on-axis digitally filtered frequency responses for both system 1 and system 2.

Note: in our experiment, the decrease of level in the $5kHz-20kHz$ frequency band is due to the low-pass filter implemented which acts as an anti-aliasing filter based on a $48kHz$ sampling frequency with $12dB$ roll-off. In practice, this amplitude decrease could be easily overcome with a high roll-off anti-aliasing filter based on a $96kHz$ sampling frequency.

3.4. Polar diagram

Since the contributions of the different drivers at a specific frequency is now defined, we proposed to look at the directional characteristics in one hand, of the separate drivers and in a second hand, of the complete system in the overlap region. Figure 9 and 10 depict respectively the simulated and measured polar diagram in the (Oy, Oz) plane of the Low-mid and Upper-mid drivers at the first theoretical crossover frequency that is to say $820Hz$. Even if the simulations is not able to describe exactly the directional characteristics of the drivers, the predictions is fairly reasonable considering the theoretical assumptions, especially in the $\pm 60^o$ solid angle. The

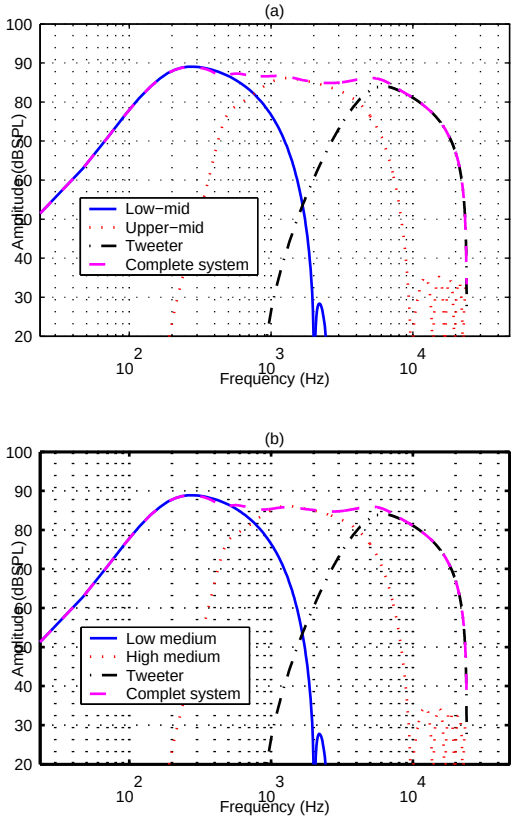

Fig. 8: Digitaly filtered loudspeaker systems : (a)-System 1 (b)-System 2

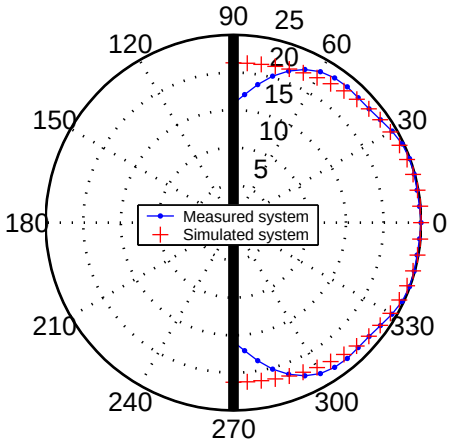

Fig. 9: Simulated and measured polar diagram of the Low-mid driver at $820Hz$

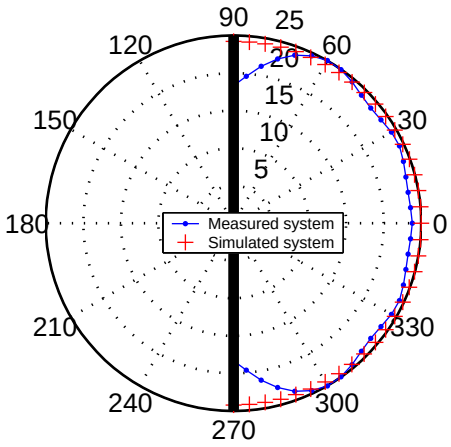

Fig. 10: Simulated and measured polar diagram of the Upper-mid driver at $820Hz$

deviation outside this range can manifestly be attributed to the border effects of the baffle when the microphone stay close to its edge. Additionally, the visible ripples within the $\pm 60^o$ solid angle may be explained by diffraction effects due to the limited size of the experimental baffle [14].

The same conclusions can be observed on the polar diagram of the complete system on figure 11. Note that polar diagram in this case of a co-incident annular rings distribution is homogenous without accident in the radiation pattern while this is no longer valid for a discrete geometrical distribution configuration. Indeed, figure 12 shows serious lobbing in the 330^o direction due to the combination of delay coming from separation of drivers and phase difference between drivers. It should be noted that this lobbing is serious even with the use of phase shifts-free digital crossover. This observation also demonstrates that the drivers cannot be considered as in-phase sources. Some crossover techniques add extra delays in order to redirect the main lobes on axis [8], [16]. The D'Appolito geometrical configuration [17] could also be used to reach this target. However, those corrections and their combinaison could not completely solve dips due to the interference problems since these defects are inherent to the driver geometrical distribution.

Even if direct comparison between simulated and

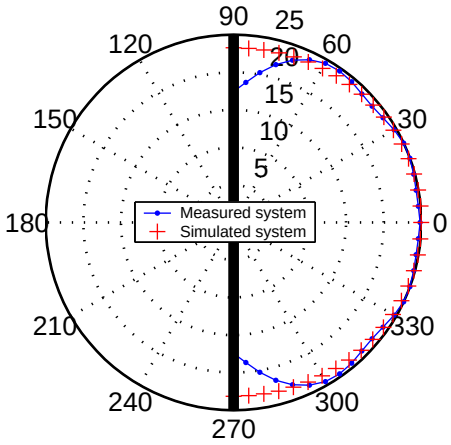

Fig. 11: Simulated and measured polar diagram of the complete co-incident system at $820Hz$

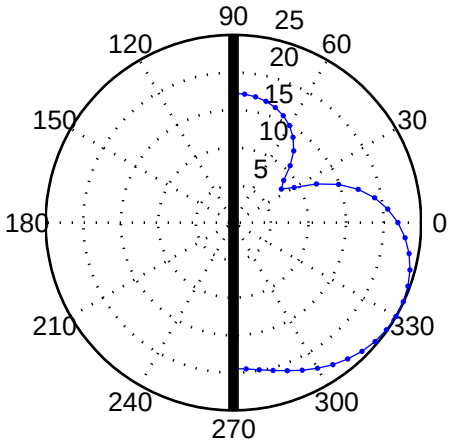

Fig. 12: Simulated polar diagram of the discrete geometrical system at $820Hz$

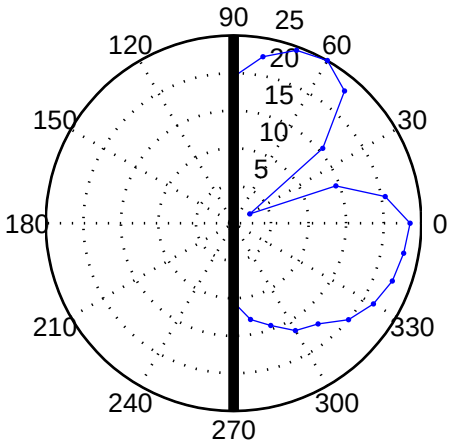

Fig. 13: Measured polar diagram of the typical discrete geometrical system at $800Hz$

measured results are not possible (since exact system 2 is not available), similar phenomena are visible on the real discrete geometrical configuration measured which is using two Low-mid and one Upper-mid driver (see figure 13).

On the opposite, this phase shifts between drivers has no incidence of the direction of maximum energy which is still on axis in the case of the co-incident ring distribution.

Figure 14 and 15 shows the directivity of the Upper-mid and Tweeter in the second crossover frequency at $4100Hz$. Comparisons between simulations and measurements are pretty consistent even for the Upper-mid driver. Deviation for the tweeter outside the 60^o solid angle is also due to the edge of the experimental limited baffle. Within the 60^o solid angle, the ripple in this measurement results from diffraction effects and the existence of a short waveguide not taken into account in our model.

At the second crossover frequency, the polar pattern of the system depicted in figure 16 remains smooth and homogenous. Despite of still imperfect predictions, the simulation provides interesting trends of the radiation characteristics of the source.

Applying the same method for the equivalent discrete geometrical distribution leads to the polar response of figure 17. One more time, serious lobbing

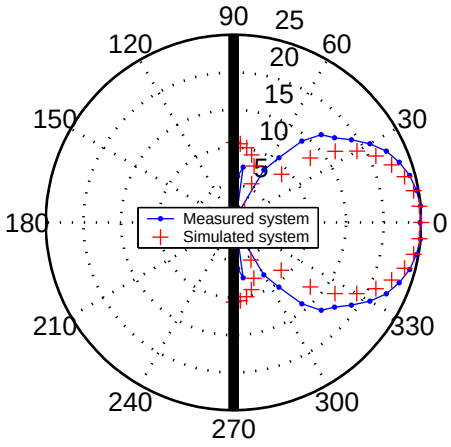

Fig. 14: Simulated and measured polar diagram of the Upper-mid driver at $4100Hz$

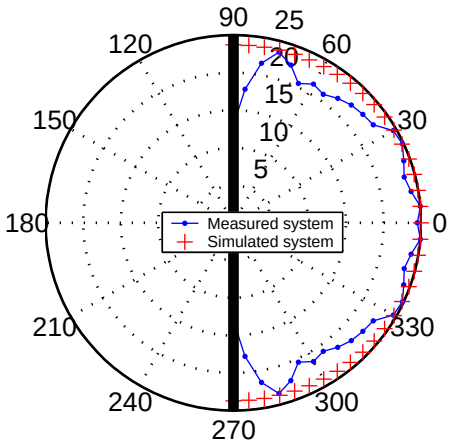

Fig. 15: : Simulated and measured polar diagram of the tweeter at $4100Hz$

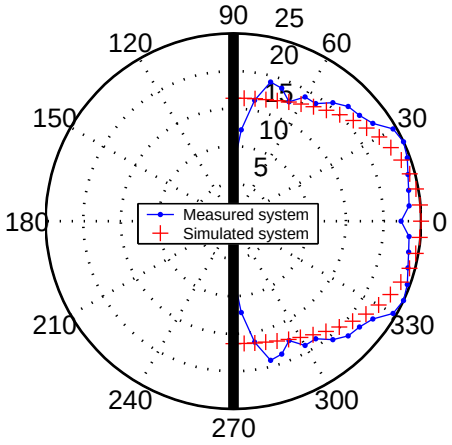

Fig. 16: Simulated and measured polar diagram of the complete co-incident system at $4100Hz$

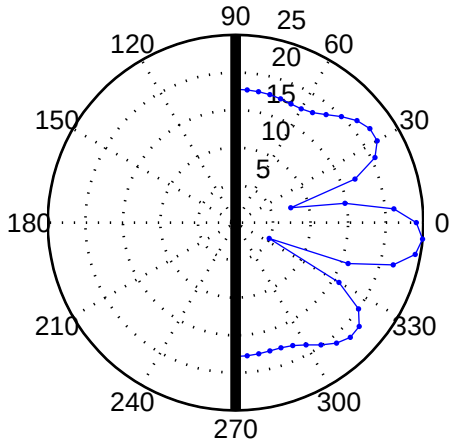

Fig. 17: Simulated polar diagram of the discrete geometrical system at $4100Hz$

and direction of nulls are illustrated revealing significant interference problems.

Comparison with a measured discrete geometrical configuration (but unfortunately not exactly equivalent to system 2) at the upper-mid/tweeter crossover frequency exhibits similar weakness (see figure 18).

Finally, figure 19 shows the phase response over 2π angle of co-incident and discrete distributed configuration at $820Hz$ and $4100Hz$. The phase of the co-incident source is very stable at both frequencies when a listener is moving in the (Oy, Oz) plane and keep the same distance to the source. On the opposite, the phase is changing rapidly around the on-axis direction in the discrete geometrical distribution. Even if, at that frequencies, the phase shift fluctuation remains negligible compared to a phase shift due to time delay, these phase responses are useful in understanding the magnitude polar plots difference. These curves also reveals that the wavefront is very close to a spherical wave in the case of the co-incident configuration. On the contrary, the wavefront of the distributed source is largely distorted.

3.5. 2D plot map description

Polar plots are some useful tools to describe the directivity characteristics of a source. However, they are inappropriate to enhance all the details of a radi-

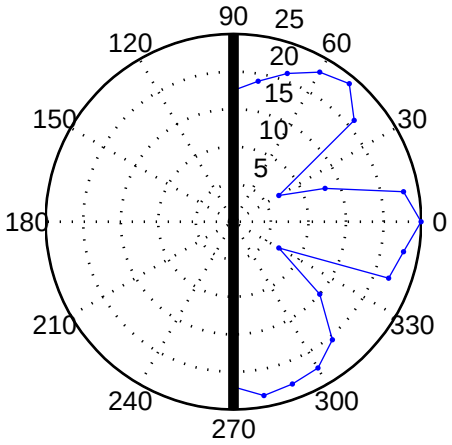

Fig. 18: Measured polar diagram of the typical discrete geometrical system at $3500Hz$

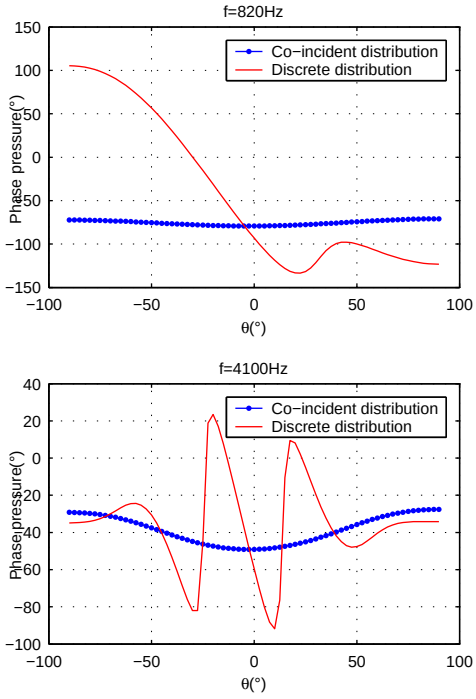

Fig. 19: Phase response simulated over 2π solid angle of co-incident and discrete distributed configuration at $820Hz$ and $4100Hz$

ation field especially in the near field region. Therefore, we suggest in the following schemes to display some $2D$ map description of the radiating field in the (Oy, Oz) plane. Applying this methodology to the co-incident and discrete geometrical distribution leads to figures 20, 21, 22 and 23 at the two crossover frequencies. The difference between the two configurations of sources on the radiated field is clearly visible. In the case of the co-incident configuration, at $f_1 = 820Hz$, the source is radiating a nearly perfect spherical wave of an ideal monopole with an $1/r$ magnitude decrease. At $f_2 = 4100Hz$, the co-incident source starts to slightly steer on axis but the radiation pattern remains extremely homogeneous even in near field. On the opposite, the discrete distribution configuration shows non-symmetrical radiation field with bright and shadow zones. At $f_2 = 4100Hz$, the interferences rays are clearly seen with serious magnitude changes even on limited portion of space. The imperfections are even more severe in the near field region (between 0.5 to $1m$) where a motion of typically $15cm$ of the listener's ears will induce $25dB$ magnitude drop at that frequency.

4. CONCLUSION

A formulation model of the sound field radiated by annular membranes has been proposed. The predictions are in fairly good agreement with measurements despite of strong assumptions (especially pistonic motions). This model provides better understanding of the way the sound wave is propagating into space. Applying this technique to investigate the radiation of a multi-way system reveals and corroborates the benefits of co-incident drivers compared to a conventional discrete geometrical distribution. The mentioned characteristics of this design make this source especially suitable for near field monitoring application. Informal listening tests proceeded with audio professionals confirm the coherency and stability of the soundstage, from far field to near field conditions.

5. FURTHER WORKS

A better model will consist in measuring the velocity along the profile of the diaphragm and alternatively, evaluate it with a Finite Element Method (FEM) software. Future works will also focus on describing the radiation of the co-incident configuration in a 4π

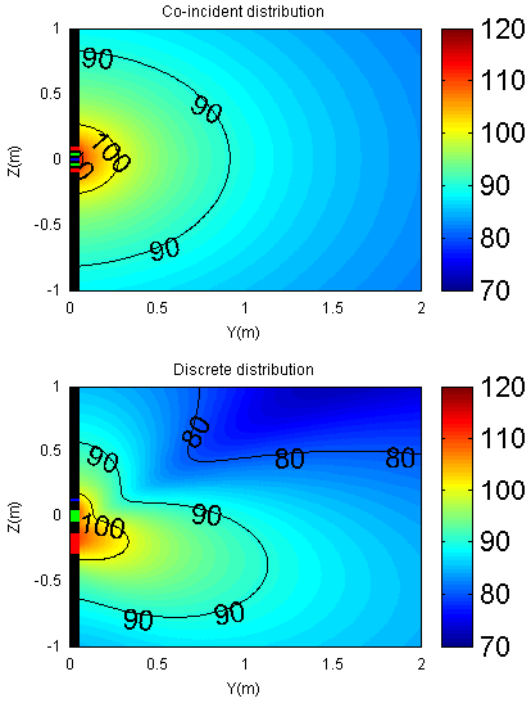

Fig. 20: Simulated $2D$ plot of the radiated field of co-incident and discrete geometrical distribution on the (Oy, Oz) plane at $820Hz$

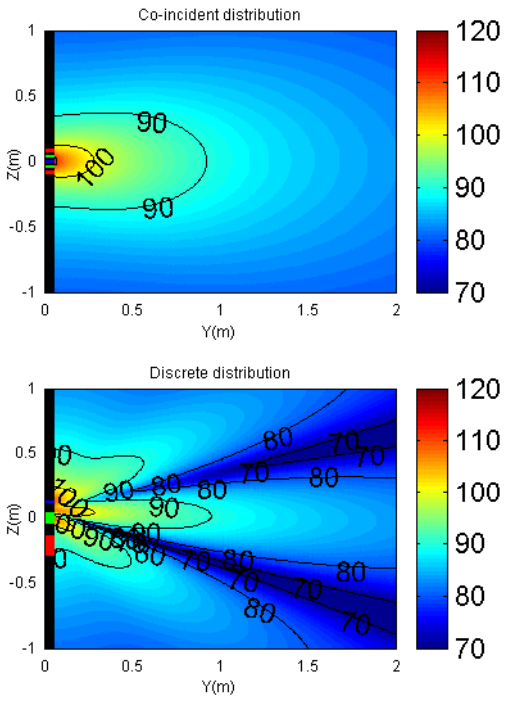

Fig. 21: Simulated $2D$ plot of the radiated field of co-incident and discrete geometrical distribution on the (Oy, Oz) plane at $4100Hz$

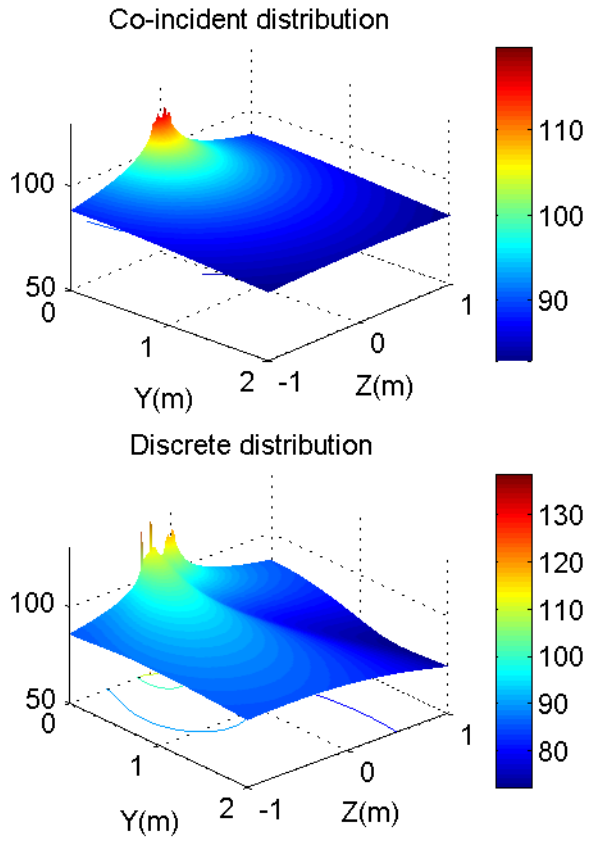

Fig. 22: Simulated $3D$ plot of the radiated field of co-incident and discrete geometrical distribution at $820Hz$

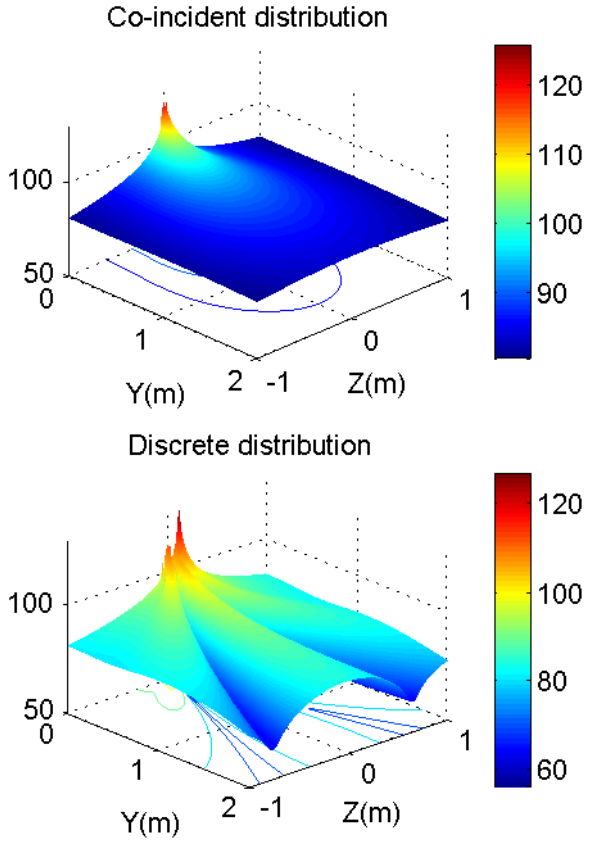

Fig. 23: Simulated $3D$ plot of the radiated field of co-incident and discrete geometrical distribution at $4100Hz$

solid angle without baffle.

6. ACKNOWLEDGEMENTS

This work was supported by Yvon KERNEIS, R&D director of the Cabasse Acoustics Center and Jean-Marc BOUCHER, Professor at the Signal and Communication department of the ENST Bretagne. The authors would like to express special gratitude to Dr. Joël RICHARD and Yvon KERNEIS who are the inventors of the three ways annular/circular coincident speaker technology described hereby in this paper.

7. REFERENCES

[1] T R. Telesky, "The design of a point source, near field reference monitor". presented at the 76th convention of the AES, New York, Oct 8-11,1974.

[2] W. Gelow, "Design consideration of a high level co-axial source". presented at the 87th convention of the AES, New York, Oct 18-21, 1989.

[3] M A. Dodd, "A wide dispersion constant directivity dual concentric driver". presented at the 92th convention of the AES, Vienna, Mar 24-27, 1992.

[4] P M. Morse and K V. Ingard, "Theoretical acoustics " Mc Graw-Hill, New York, 1968.

[5] J. Makazino, "Co-axial flat-plane loudspeaker with polymer-graphite honeycomb sandwich plate diaphragm", JAES, Volume 28, Number 11, pp 800-807, Nov 1981.

[6] M. Bruneau, "Introduction aux théories de l'acoustique", Université du Maine editor, Le Mans, France, 1983.

[7] R. Small, "Direct radiator loudspeaker System analysis", JAES, Volume 20, Number 5, pp 383-395, Jun 1972.

[8] R. Bews, "Digital crossover networks for active loudspeaker systems", PhD, University of Essex, Colchester, Sep 1987.

[9] A. Rimell, "Reduction of loudspeaker polar response aberrations through the application of psychacoustic error concealment", PhD, University of Essex, Colchester, Dec 1996.

[10] R M. Aarts, "A new method for the design of crossover filters", JAES, Volume 37, Number 6, pp 445-454, Jun 1989.

[11] R. Wilson AND R. Adams, "Application of digital filters to loudspeaker crossover", JAES, Volume 37, Number 6, pp 455-463, 1989.

[12] S P. Lipshitz AND J. Vanderkooy, "A Family of linear-phase crossover networks of high slops derived by time delays", JAES, Volume 31, Number 1/2, pp 2-20, Jan 1983.

[13] K C. Haddad et al, "Design of Digital linear-phase FIR Crossover systems for loudspeakers by the method of vector space projections", IEEE Transaction on signal processing, Volume 47, Number 11, pp 358-462, Nov 1999.

[14] B. Debail, "Etude de dispositifs de prise de son faible bruit et à sélectivité spatiale contrôlée dans le cadre de la visioconférence de groupe", PhD, Université du Maine, Le Mans, France, Nov 2000.

[15] E. Skudrzyk, "Fundamentals of Acoustics", Springer-Verlag, Wien - New York, 1971.

[16] S H. Linkwitz, "Active crossover networks for noncoincident drivers", JAES, Volume 24, Number 1, pp 2-8, Jan 1989.

[17] M D'Appolito, "A geometric approach to eliminating lobbing error in multiway loudspeakers". presented at the 92th convention of the AES, preprint 2000, 1983.

8. APPENDIX

The acoustic radiation impedance can be evaluated by considering the force acting on the ring due to the pressure contribution on elementary surface $dS"$ of the ring. Considering equation (6), the force can be written as:

$$F = \int \int_{S"} p(\vec{r}) dS"$$

that is to say :

$$F = \frac{j\,k\rho cv}{2\pi}\int_0^{2\pi} d\phi^{"}\int_{a_i}^{a_o} a^{"}\,da^{"}\int_0^{2\pi} d\phi^{'} \int_{a_i}^{a_o}\frac{e^{-jk|\vec{r}-\vec{r^{'}}|}}{|\vec{r}-\vec{r^{'}}|}a^{'}\,da^{'}$$

However, in order to simplify the model, we will considered the general approximation given in [15] with:

$$Z_{ar} = S\rho c[\frac{1}{2}(ka_{eq})^2 + j\omega\frac{8ka_{eq}}{3\pi}]$$

where a_{eq} is the radius of an equivalent disc having the same surface area than the ring of internal radius a_i and outside radius a_o.